



Tailorable morphology control of Prussian blue analogues toward efficient peracetic acid activation for sulfonamides removal

Yujie Cheng^a, Zongping Wang^a, Lisan Cao^a, Zhenbin Chen^a, Yiqun Chen^b, Zizheng Liu^b, Jun Ma^c, Pengchao Xie^{a,*}

^a School of Environmental Science and Engineering, Huazhong University of Science and Technology, Wuhan 430074, China

^b School of Civil Engineering, Wuhan University, Wuhan 430072, China

^c State Key Laboratory of Urban Water Resource and Environment, Harbin Institute of Technology, Harbin 150090, China



ARTICLE INFO

Keywords:

Advanced oxidation processes
Peracetic acid activation
Structure-activity relationship
Organic radicals
Bimetal synergic effect

ABSTRACT

Herein, the relationship between defined morphologies of Prussian blue analogues and their catalytic properties is comprehensively investigated. Solid Co-Fe-Cube and three different hollow morphologies (Box, Cage, and Frame) were successfully synthesized and exhibited distinct activation performance toward peracetic acid. The evolution of hollow interior led to partial disassociation of porous nanostructure, while Co-Fe-Cube with its solid cubic feature, high specific surface area (222.3 m²/g), and excellent stability (minimal leakage of metal ions) achieved the best removal efficiency (around 90 %) of six sulfonamides in 15 min. Organic radicals including CH₃CO₃[•] and CH₃CO₂[•] are identified to play the dominant role, and Co-Fe bimetal synergic effect induces the regeneration of highly active \equiv Co(II) sites. This work provides new insights into the structure-activity relationship and paves the way for precise structure control and property modulation of advanced catalysts in water decontamination.

1. Introduction

Sulfonamides (SAs) are commonly used antibiotics in human medicine and livestock farming. Discharged SAs and their metabolites are frequently detected in the aquatic environment worldwide, leading to the global dissemination of antibiotic resistance [1,2]. Conventional biological processes in wastewater treatment plants have been proven to be inefficient in eliminating SAs due to their antimicrobial property [3, 4]. Consequently, SAs have raised extensive concerns regarding their potential threats to both ecosystems and human health. Advanced oxidation processes (AOPs) are considered one of the most promising technologies to eliminate refractory organic pollutants due to the generation of highly-oxidative radicals (HO[•], SO₄²⁻, O₂[•], etc.) and highly-selective nonradicals, such as ¹O₂ and Fe(IV) [5].

In recent years, peracetic acid (PAA), the emerging disinfectant for decontamination and inactivation, has attracted increasing attention in AOPs due to its lower O-O bond dissociation energy (159 kJ mol⁻¹) than H₂O₂ (213 kJ mol⁻¹) and the generation of highly-oxidative organic radicals (RO[•]), such as CH₃CO₃[•] and CH₃CO₂[•] [6,7]. PAA can be effectively activated by energy input (UV, ultrasound, heat) and transition

metallic ions (Co(II), Fe(II), Ru(II)) [8]. However, homogeneous processes are usually plagued by some inherent disadvantages, including expensive energy cost, precipitation of metal salts, toxicity of leaked ions, and difficulty in catalyst recycling [9]. Therefore, researchers deflect to look for viable heterogeneous materials, and numerous candidates with high efficiency in PAA activation have been developed. Nevertheless, the rational design of catalysts with the defined structure and excellent morphology is usually ignored in most of previous research, which is crucial to help us understand the intricate correlation between the material structure and the catalytic property.

Prussian blue analogues (PBAs) are representative cyanide-bridged coordination polymers and constitute a subclass of metal organic frameworks (MOFs) [10]. PBAs exhibit great potential for molecular-level tuning in their structures, providing opportunities to explore the structure-activity relationship [11]. Their chemical formulas are typically expressed as A_xM_A[M_B(CN)₆]_y • zH₂O or M_A[M_B(CN)₆]_x • yH₂O, where A represents alkali cations, such as Na⁺ and K⁺, intercalated into the frameworks, M_A and M_B correspond to the transition metal ions coordinated to the cyano groups [12]. PBAs possess several appealing properties that make them ideal candidates for

* Corresponding author.

E-mail address: pengchao_xie@hust.edu.cn (P. Xie).

activating peroxides in AOPs [13,14]. These include a three-dimensional porous framework that ensures the uniform dispersion of active sites, open channels that greatly facilitate the diffusion and transport of contaminants, and dual transition metal sites (M_A and M_B) that can interact to trigger a synergistic effect. The flexible synthesis of PBAs makes it possible to manufacture diverse crystalline shapes, compositions and morphologies with different catalytic properties [15]. PBAs have been employed to activate peroxides in the past few years [16–20]. Some literature reported the PAA activation with other Co or Fe containing catalysts, unveiling the removal efficiency of contaminants and the generation process of dominant ROS [21–23]. However, previous studies on the relationship between the catalyst structure and the activation performance on peroxides (structure-activity relationship) are limited. Additionally, no report focusing on the PBAs in PAA-based AOPs has been found.

Most of previous literature achieved the morphological control of PBAs by additional etchants or extra treating procedures, which makes the large-scale preparation difficult in practical industrial processes [14, 15]. In this study, we employed a one-pot aqueous precipitation method to tune the growth kinetics of Co-Fe PBAs, achieving the facile in-situ control over four tailorabile morphologies including box, cage, frame, and cube. The phase transition of Co-Fe PBAs during the synthetic process was carefully investigated, and the catalytic performance of different morphologies was compared through a perspective of structure-activity relationship. The in-depth mechanism including the identification of dominant reactive oxidative species (ROS) and the Co-Fe bimetal synergic effect was revealed. Additionally, degradation pathways and biotoxicity variation of sulfamethoxazole (SMX) was disclosed, highlighting the promising potential of finely tuned Co-Fe-PBAs in practical water treatment.

2. Materials and methods

2.1. Chemicals and reagents

All chemicals utilized in this study were of analytical grade at least without further purification unless otherwise stated, and details were provided in Text S1. The synthetic procedure of PAA stock solution was illustrated in Text S2.

2.2. Synthesis of Co-Fe-PBAs

The morphology control of Co-Fe-PBAs was achieved by adjusting the synthetic temperature and the dosage of surfactants according to previous literature with modification [24,25]. For Co-Fe-Cube, a solution of 0.66 g potassium hexacyanoferrate in 100 mL ultrapure water was added into a solution of 0.75 g cobalt acetate tetrahydrate and 1.3 g trisodium citrate dihydrate in 100 mL ultrapure water. After magnetic stirring for 2 min, the mixed 200 mL solution was aged at 20 °C for 24 h. The obtained violet precipitate was collected by centrifugation and washed with ethanol and ultrapure water for three times, respectively. The detailed procedures of other Co-Fe-PBAs, Co-Co-PBA, and Fe-Fe-PB are provided in Text S3.

2.3. SAs degradation

100 mL conical flask was used to conduct batch experiments. The magnetic stirring rate was 300 r min⁻¹ and the reaction temperature was 25 ± 1 °C. The initial pH value was adjusted to 6.7–7.0 immediately using H₂SO₄ and NaOH after the addition of SAs and PAA. Then reaction began after the addition of catalyst. The variation of pH during the 15 min reaction was less than 0.4, so no buffer solution was used to avoid unnecessary interference. The aliquots (1 mL) were withdrawn at pre-determined time intervals, then quenched by 10 μL 0.5 M Na₂S₂O₃ and filtered through a 0.22 μm acetate fiber membrane for further analysis. The detailed illustration of analytic methods was provided in Text S4.

2.4. Materials characterization

The morphologies of the catalysts were investigated by scanning electron microscopy (SEM, JEOL JSM-IT 200) and transmission electron microscopy (TEM, FEI Tecnai G2 F20). X-ray energy-dispersive spectroscopy (EDS) mappings were conducted by using Oxford X-PIRE detector. The crystal structure of Co-Fe-PBAs was confirmed by X-ray diffraction (XRD, Shimadzu, XRD-7000) with Cu-K α radiation, and the element composition was investigated by X-ray photoelectron spectroscopy (XPS, Thermo Scientific ESCALAB Xi+). Fourier transform infrared spectroscopy (FTIR) were collected on a Bruker VERTEX 70 v spectrometer. Brunauer-Emmett-Teller (BET) specific surface area and pore volume was obtained by Micromeritics ASAP 2460 instrument. Inductively coupled plasma optical emission spectrometer (ICP-OES, Optima 8300, Perkin Elmer, USA) was used to measure the leakage of Co and Fe ions.

3. Results and discussion

3.1. Morphology control of Co-Fe-PBAs

Fig. S1 in the supplementary material provided a schematic illustration of the one-pot synthetic route used in this study, and Fig. 1 displayed SEM and TEM images of Co-Fe-Box, Cage, Frame, and Cube, along with their corresponding schematic models in the upper right corner. The nucleation rate of Co-Fe-PBAs was finely controlled by adjusting the synthetic temperature and the dosage of surfactants (details in Text S5), including trisodium citrate dihydrate and polyvinylpirrolydone, to regulate their crystallinity [26]. As a result, all the products exhibited uniform and high-quality geometry with an average size of approximately 150–200 nm. Fig. 1a showed the well-defined cubic crystals, while some irregular voids (marked with red circle) existed on the surface of several crystals, suggesting that the interior of Co-Fe-Box may be empty. The TEM image in Fig. 1e confirmed the presence of the closed single-shelled hollow structure. In addition, we found that PBA at the first 2 min mixture stage (named PBA-2 min in Fig. S1) exhibited an intact and solid structure in Fig. S2, suggesting that the interior core of Co-Fe-Box gradually dissolved during the ripening process [27]. The well-defined cavities at the eight corners of Co-Fe-Cage were clearly visible in Fig. 1b, while Co-Fe-Frame exhibits cavities located at the center of six {1 0 0} facets, which was in line with the open hollow structure observed in TEM images (Fig. 1f,g). The shells of the three hollow catalysts were approximately 40 nm thick, while the Co-Fe-Cube in Fig. 1d,h showed a solid cubic structure without any hollow features. The high-resolution TEM (HRTEM) image in Fig. 1i showed the distinct lattice fringes of Co-Fe-Cube, and the interplanar spacing of 0.267 and 0.529 nm corresponded to the {4 0 0} and {2 0 0} facets of Co-Fe-PBAs, respectively [25]. The Co-Fe-Cube possessed a high-quality single crystalline nature as confirmed by its clear selected area electron diffraction (SAED) pattern in Fig. 1j. The consistent HRTEM images and SAED patterns for other as-prepared PBAs were shown in Figs. S3 and S4, demonstrating their identical constitution and single crystalline nature. Surprisingly, the high-angle annular dark-field scanning transmission electron microscopy (HAADF-STEM) and EDS images in Fig. 1k revealed the uniform distribution of Co, Fe, and K elements, which is inconsistent with the typical composition of Co₃[Fe(CN)₆]₂ [13]. These results suggest a possible introduction of K⁺ from the ingredient (potassium hexacyanoferrate) to the porous framework of Co-Fe-PBAs, which will be discussed in detail in the next section. Overall, all four PBAs with tailorabile morphologies were successfully in-situ constructed without additional etchant or extra treating procedure, demonstrating the feasibility of the one-pot aqueous precipitation method to subtly control the catalyst geometry.

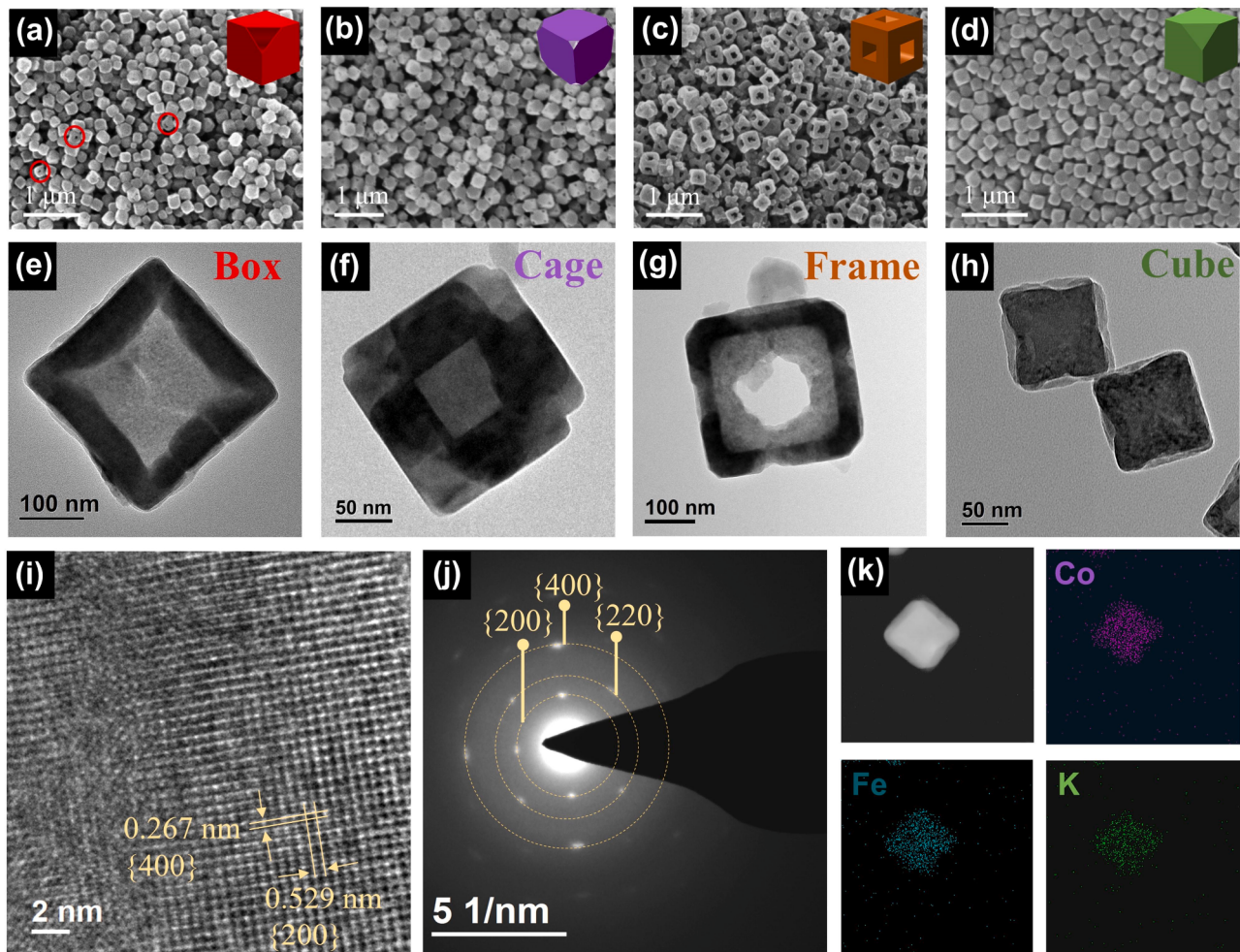


Fig. 1. (a-d) SEM and (e-h) TEM images of the Co-Fe-Box, Cage, Frame and Cube. Insets of (a-d) in the upper right corner are corresponding schematic models. (i) HRTEM, (j) SAED, (k) HAADF-STEM micrographs and EDS elemental mapping of Co-Fe-Cube.

3.2. Phase transition and intramolecular electron transfer

Fig. 2a displayed the color change of PBAs during the ripening process. Before the ripening stage (stage II in Fig. S1), PBA-2 min presented a brownish color, which eventually turned violet for all Co-Fe-PBAs. The violet spectral lines of K element suggest the incorporation of K^+ into the material composition along with possible phase transitions [28]. PBA-2 min shared the same solid cubic morphology as Co-Fe-Cube in Fig. S2. However, the EDS analysis in Fig. S5 revealed a significantly lower proportion of K in PBA-2 min compared to Co-Fe-Cube, with atomic ratio (K: Fe) of 0.1 and 0.5, respectively. This indicated the migration of K^+ from the solution into the porous structure of PBAs during the ripening process. Notably, Co-Fe-Cage, Box, and Frame exhibited a higher K: Fe atomic ratio of approximately 1:1 in Fig. S5a-c, which might be attributed to the faster K^+ migration rate at higher synthetic temperature (20 °C for Cube, 50 °C for Frame, and 80 °C for Cage and Box) [27].

XRD patterns were measured to further verify the process of phase transition. As illustrated in Fig. 2b, the characteristic peaks of PBA-2 min were assigned to the standard pattern of $Co_3[Fe(CN)_6]_2$, denoted as CoFe phase. While the Cube-4 h exhibited a shift of the peaks toward the higher diffraction angle after 4 h of ripening, indicating the incorporation of K^+ into the porous nanostructure. The new phase was ascribed to $K_2CoFe(CN)_6$, hereafter referred to KCoFe phase [29]. All four final Co-Fe-PBAs present the pure KCoFe phase, indicating the complete phase transition. Fig. 2c exhibited the face-centered cubic crystal

structure of KCoFe phase. The carbon-coordinated $\equiv Fe$ sites and nitrogen-coordinated $\equiv Co$ sites are bridged by cyanide groups (CN) to form a three-dimensional open framework. Additionally, the porosity and the rigid cubic coordination network offer extensive interstitial open sites, which can be intercalated by water molecules and alkali metal ions [12]. On the basis of foregoing analysis, the incorporation of K^+ into the framework structure, along with the transition from CoFe phase to the new KCoFe phase, can be confirmed undoubtedly.

Previous literature reported that the insertion of K^+ and OH^- into the framework of PBAs can trigger a proton-coupled electron transfer (PCET) reaction [30,31]. The ligand water coordinates to $\equiv Co(II)$ site (divalence from $Co(CH_3COO)_2$) to generate $\equiv Co(II)-H_2O$, which acts as both a proton donor toward the absorbed OH^- and an electron donor toward $\equiv Fe(III)$ through the cyanide bridge [25]. This leads to intramolecular electron transfer and the transformation from $Co(II)-N\equiv C-Fe(III)$ to $Co(III)-N\equiv C-Fe(II)$. To determine whether the $\equiv Fe$ sites varied from trivalence in the ingredient $K_3Fe(CN)_6$ to divalence in the prepared Co-Fe-PBAs, FTIR analysis was conducted and shown in Fig. 2d. The peaks at 3639 and 3411 cm^{-1} were associated with the absorbed OH^- and ligand water in the pore channel of framework structure. The v(CN) peaks at 2158, 2119 and 2102 cm^{-1} were ascribed to $Co(II)-N\equiv C-Fe(III)$, $Co(III)-N\equiv C-Fe(II)$ and $Co(II)-N\equiv C-Fe(II)$, respectively [27]. Obviously, the peaks representing $\equiv Fe(III)$ at 2158 cm^{-1} was apparent in PBA-2 min but disappeared in Co-Fe-Cube after 24-hour aging. The absence of the 2158 cm^{-1} peak was also observed in the FTIR spectra of Co-Fe-Cage, Box, and Frame (Fig. S6), demonstrating that all the $\equiv Fe$

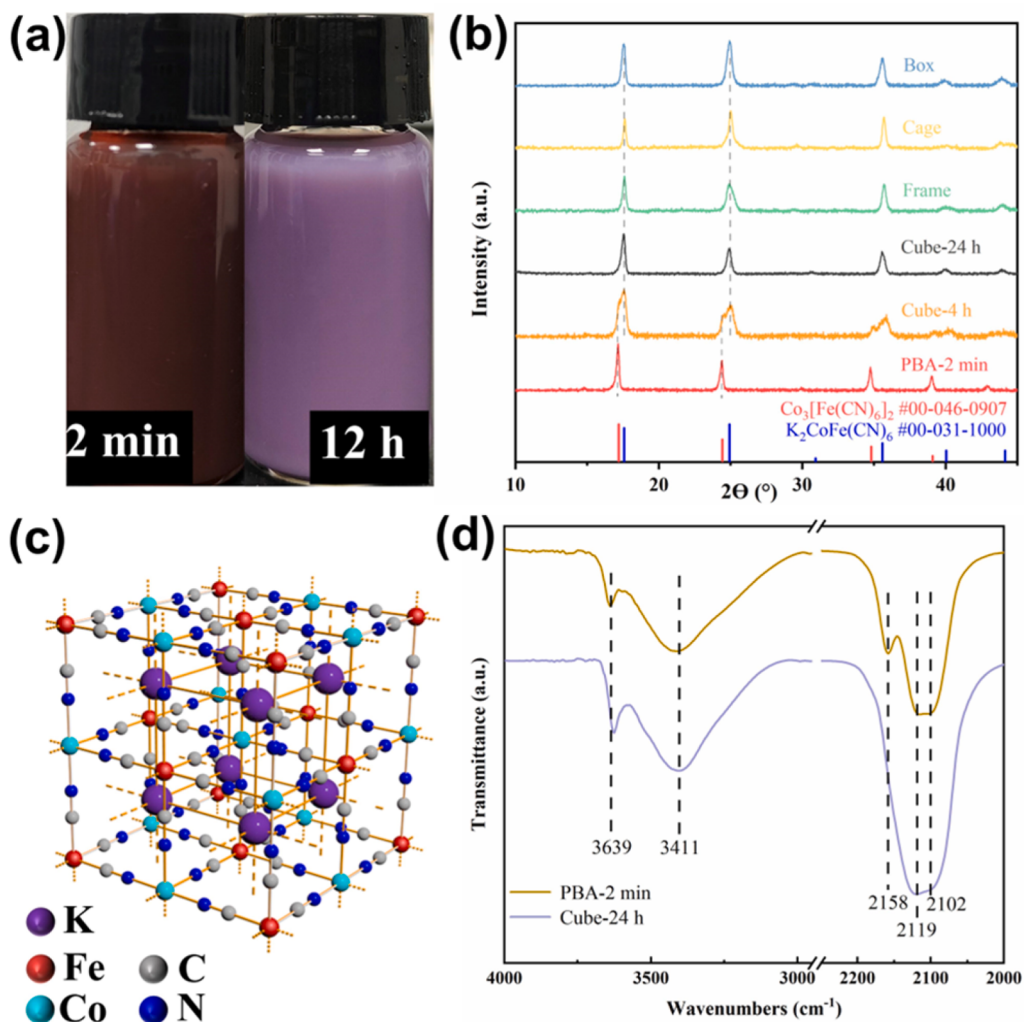


Fig. 2. (a) Color variation during the ripening process of PBAs. (b) XRD patterns of PBAs under different synthesis conditions. (c) Crystal structure of PBAs with interstitial sites occupied by K^+ . (d) FTIR spectra of Co-Fe-Cube and PBA-2 min.

(III) sites in the prepared PBAs are reduced to $\equiv\text{Fe}(\text{II})$. Furthermore, the XPS spectra of Co-Fe-Cube in Fig. 5b showed a single peak of $\equiv\text{Fe}(\text{II})$ along with a mixture of $\equiv\text{Co}(\text{II})$ and $\equiv\text{Co}(\text{III})$, also indicating the process of intramolecular electron transfer. Considering that $\equiv\text{Fe}(\text{II})$ activates PAA much faster than $\equiv\text{Fe}(\text{III})$, the reduction of $\equiv\text{Fe}(\text{III})$ to $\equiv\text{Fe}(\text{II})$ is expected to enhance the catalytic performance [32]. In brief, we successfully fabricated four brand-new Co-Fe-PBAs with KCoFe phase and diverse morphologies, in which the $\equiv\text{Co}(\text{II})$, $\equiv\text{Co}(\text{III})$, and $\equiv\text{Fe}(\text{II})$ sites are believed to activate PAA efficiently.

3.3. Efficient PAA activation for SAs degradation

To investigate the impact of diverse morphologies on PAA activation performance, SMX was chosen as the target contaminant, and its removal efficiency was compared. Three hollow Co-Fe-PBAs are expected to perform better than Co-Fe-Cube due to the feature of hollow interior, which benefits the contaminant diffusion and mass transfer [33]. However, Fig. 3a showed the 60.4 %, 74.8 %, 82.3 %, and 86.7 % degradation in 10 min for Co-Fe-Box, Cage, Frame, and Cube, respectively. Considering that the common drawback of MOFs is instability in aqueous solution, the leached Co and Fe ions were measured by ICP-OES [11]. Only 0.75 μM Co and 0.48 μM Fe were detected for Co-Fe-Cube, which is quite lower than the permissible limit of industrial wastewater in Chinese National Standard (GB 25467–2010, 1 mg L^{-1} for Co). In contrast, the leached concentrations of other three hollow Co-Fe-PBAs

were much higher, as shown in Fig. 3a. This may be attributed to that the formation of hollow interior and surface cavities damages the stable framework structure, making the original porous construction easy to collapse in water. Thus, the correlation between morphologies and stability of three hollow Co-Fe-PBAs is taken into consideration for further exploration.

The Co-Fe-Cage with eight cavities at the corners exhibited an unstable feature by releasing the highest concentration of 9.54 μM Co and 7.01 μM Fe in 10 min. Co-Fe-Frame possessed six cavities at the center of six {1 0 0} facets, and its leached concentration was less (5.98 μM Co and 3.87 μM Fe). Additionally, Co-Fe-Box with no defects on the surface released 3.62 μM Co and 2.84 μM Fe, which appeared to be relatively stable and roughly supported the above hypothesis. The N_2 adsorption-desorption isotherms of four PBAs were measured to further evaluate the intrinsic difference in porosity. As indicated in Fig. 2b and Table S2, the Co-Fe-Cube owned a significantly higher BET surface area and pore volume than other catalysts. All four Co-Fe-PBAs presented a typical type IV isotherm, and the hysteresis loops in the range of 0.8–1.0 P/P_0 indicated the existence of mesopores. The Fig. S7 displayed the pore size distribution of four catalysts, and all four Co-Fe-PBAs exhibited micropore and mesopore features. However, the amount of micropore in Co-Fe-Cube was much higher, providing convincing evidence that the microporous structures of Co-Fe-PBAs were partly destructed during the evolution of hollow construction. High BET surface area indicates the existence of abundant active catalytic sites on the

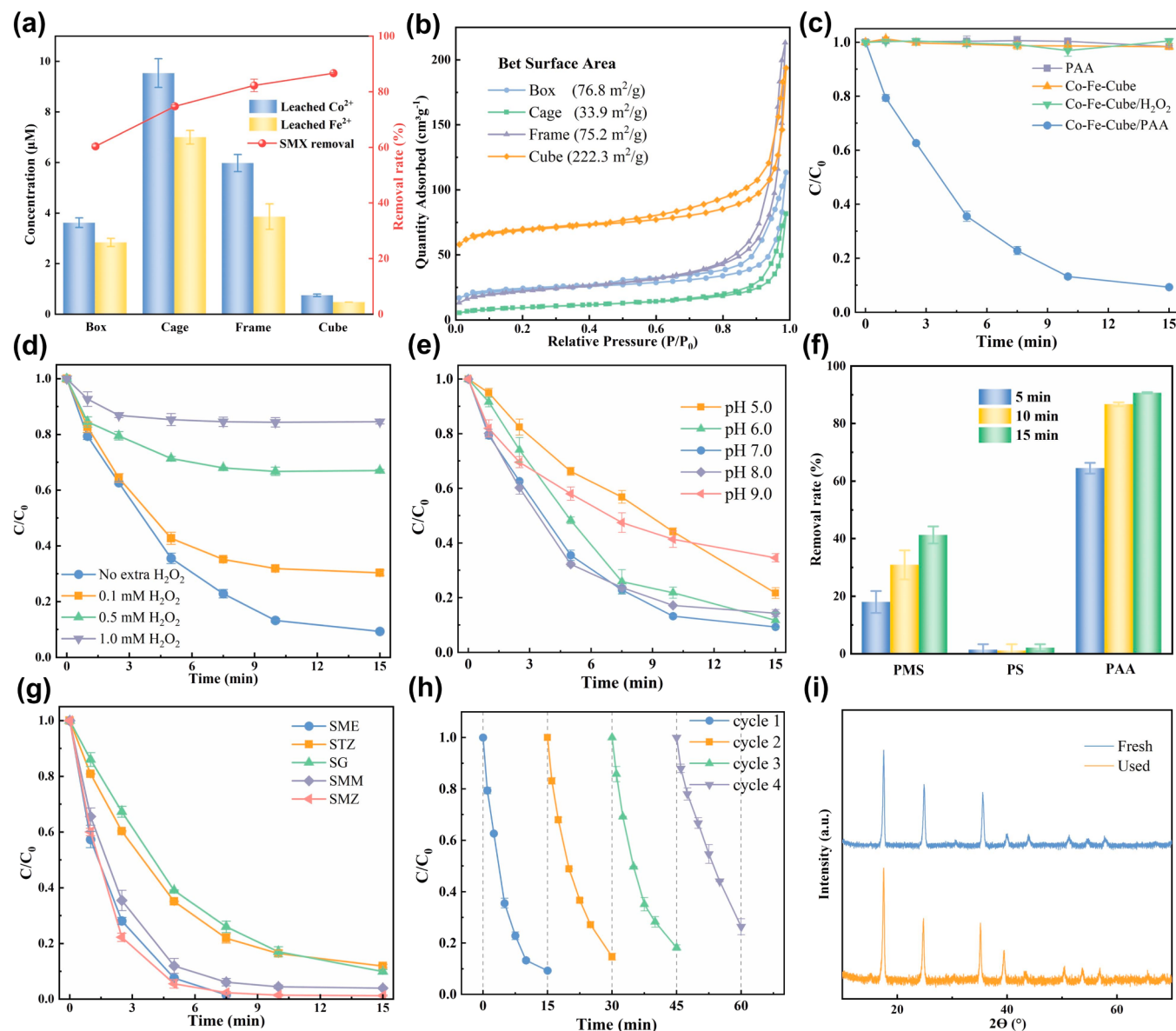


Fig. 3. (a) Metal ions leaching and SMX degradation performance of four Co-Fe-PBAs. (b) N_2 adsorption-desorption isotherms of four Co-Fe-PBAs. (c) Comparison of SMX degradation in different processes. Effects of different (d) extra addition of H_2O_2 , (e) pH and (f) peroxides on SMX removal. (g) Degradation of different SAs, (h) reusability tests and (i) change of XRD pattern in the Co-Fe-Cube/PAA process. Conditions: $[\text{PAA}] = [\text{H}_2\text{O}_2] = [\text{PMS}] = [\text{PS}] = 100 \mu\text{M}$, [catalyst] = 40 mg L^{-1} , [SAs] = $10 \mu\text{M}$, temperature 25°C .

surface of Co-Fe-Cube, which benefits PAA activation and SAs elimination. Therefore, Co-Fe-Cube/PAA process was chosen to further investigate its efficiency and mechanism, as it achieved the best SMX degradation performance along with the lowest leached metal ions.

As illustrated in Fig. 3c, $100 \mu\text{M}$ PAA alone could not degrade SMX directly, suggesting its poor oxidative capability toward SMX without activation. Moreover, the contribution of physical adsorption was negligible, as no removal of SMX was observed for Co-Fe-Cube alone. However, the Co-Fe-Cube/PAA process achieved over 90 % removal of SMX, indicating its excellent catalytic performance. The pseudo first-order model was introduced to describe the SMX degradation (Text S7 and Table S3), and the corresponding observed rate constant (k_{obs}) was 0.087 min^{-1} . It should be noted that PAA solution contained coexisted H_2O_2 , which might also be activated by Co-Fe-Cube to generate HO^\bullet or serve as a scavenger for ROS [34,35]. Hence, it's essential to elucidate the actual role of coexisted H_2O_2 ($62 \mu\text{M}$ when PAA dosage is $100 \mu\text{M}$ in this study). No SMX was degraded in the Co-Fe-Cube/ H_2O_2 process,

excluding the possible activation of H_2O_2 by Co-Fe-Cube. Fig. S8 monitored the variation of PAA and H_2O_2 concentration during the 15 min reaction. The results showed that approximately 90 % of PAA and 40 % of H_2O_2 were consumed, suggesting that PAA rather than H_2O_2 was the primary source of ROS. The effects of H_2O_2 were further evaluated by adding extra H_2O_2 into the Co-Fe-Cube/PAA process, and obvious inhibition of SMX degradation was observed in Fig. 2d. The removal efficiency decreased from 69.7 % to 15.4 % as the H_2O_2 concentration increased from $100 \mu\text{M}$ to 1 mM , indicating that coexisted H_2O_2 acts as a scavenger rather than a source of ROS, and the directed activation toward PAA can be achieved in the Co-Fe-Cube/PAA process.

Fig. 3e illustrated the effects of initial pH on the catalytic performance of Co-Fe-Cube/PAA process. The results showed that SMX could be efficiently degraded in the pH range of 5.0–9.0, especially in the near neutral condition (pH 6.0–8.0) with the removal rate of approximately 90 %. Other peroxides including peroxymonosulfate (PMS) and persulfate (PS) were chosen for comparison, and Fig. 3f exhibited that Co-Fe-

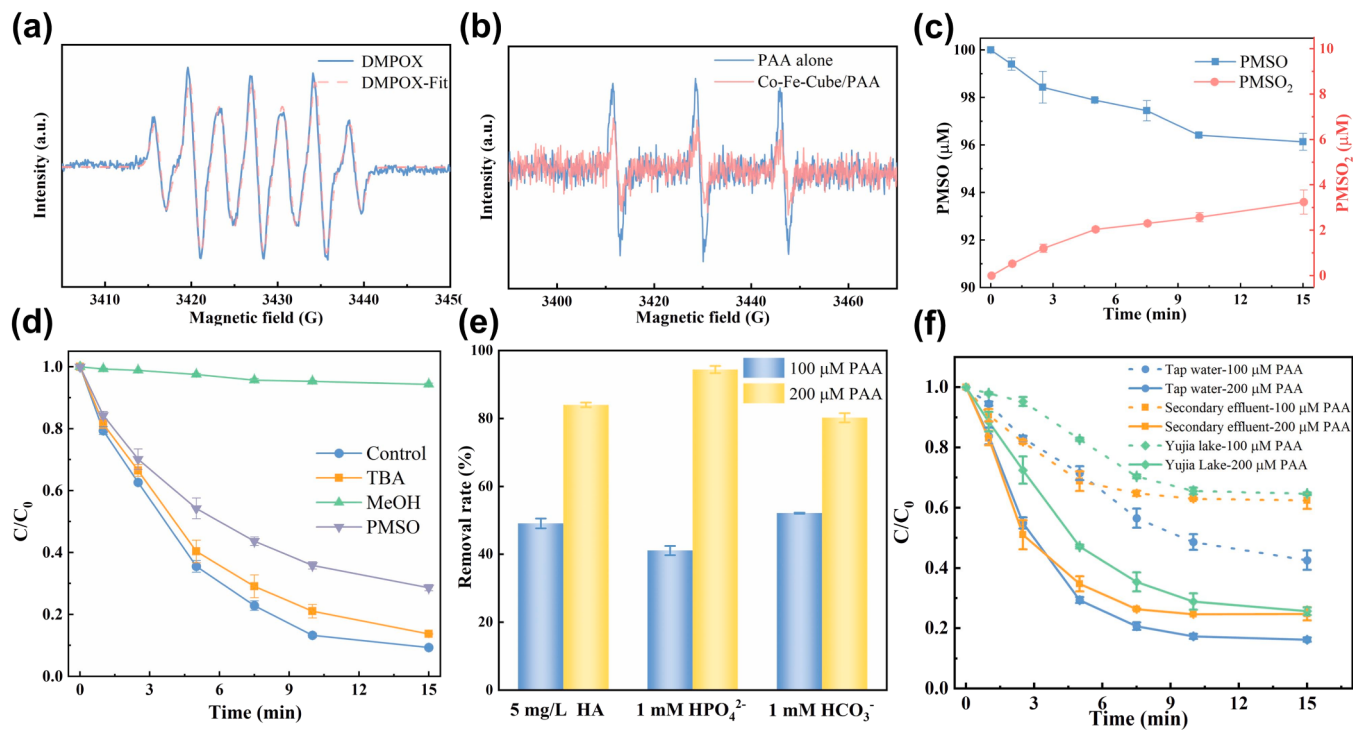


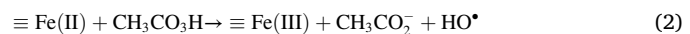
Fig. 4. (a-b) EPR spectra using DMPO and TEMP as trapping agents. (c) Oxidation of PMSO and production of PMSO₂. Effects of (d) different scavengers, (e) water matrices and (f) types of actual water on SMX degradation in the Co-Fe-Cube/PAA process. Conditions: [PAA] = 100 μM, [catalyst] = 40 mg L⁻¹, [PMSO] = 100 μM in (c) and 1 mM in (d), [SMX] = 10 μM, [TBA] = 10 mM, [MeOH] = 100 mM, [DMPO] = [TEMP] = 100 mM, temperature 25 °C.

Cube barely activates PS. Co-Fe-Cube/PMS process removed 40 % SMX in 15 min, which was far less than that of 90 % in the activated PAA process. The catalytic performance of Co-Fe-Cube/PAA process was further investigated by testing the degradation efficiency of other five commonly used SAs, including sulfamer (SME), sulfathiazole (STZ), sulfaguanidine (SG), sulfamonomethoxine (SMM), and sulfamerazine (SMZ). The results presented in Fig. 3g demonstrated that all the SAs were efficiently degraded within 15 min, indicating the extraordinary oxidizing capacity of Co-Fe-Cube/PAA process in removing SAs. The effects of PAA concentration and catalyst dosage were presented in Fig. S9 and illustrated in Text S8. Fig. S10 explored the metal ions leaching of Co-Fe-Cube/PAA process. The concentration of leached Co and Fe ions was below detection limit within 1 min, which gradually increased and reached the maximum (0.75 μM Co²⁺ and 0.48 μM Fe²⁺) at 10 min. Then the contribution of maximum leached Co and Fe ions has been explored in Fig. S11. Although the homogeneous process removed approximately 50 % of SMX, the leached ions were gradually released from catalyst surface and accumulated in solution. Consequently, the actual contribution of leached ions to SMX degradation should be significantly lower than that of the maximum leached Co²⁺-Fe²⁺/PAA process in Fig. S11, and the heterogeneous activation is considered to play a dominant role.

An ideal catalyst in AOPs should not only exhibit excellent removal efficiency but also possess robustness and recyclability [36]. Thus, the reusability of Co-Fe-Cube was examined through successive recyclability experiments in Fig. 3h. More than 70 % removal of SMX could still be achieved after four consecutive runs, and the XRD pattern of the used catalyst showed no obvious changes (Fig. 3i), demonstrating the structure stability and application feasibility of Co-Fe-Cube. The thermal behavior of Co-Fe-Cube was investigated by thermogravimetric analysis in Fig. S12. The weight loss in first stage (below 200 °C) is attributed to the removal of crystalline and coordinated water, and the organic ligands begin to decompose over 300 °C [13].

3.4. Identification of ROS in the Co-Fe-Cube/PAA process

The \equiv Co and \equiv Fe active sites on the surface of Co-Fe-Cube both participate in PAA activation via Eqs. (1-7) and produce multiple ROS. Efficient Co(II)/Co(III) redox cycle can be achieved, while \equiv Fe(III) barely activates PAA for the slow reaction rate [21,32]. The homolytic cleavage of O-O bond produces highly oxidative radicals including HO[•] and RO[•] (CH₃C(O)O[•], CH₃C(O)OO[•]). The O-O bond of PAA might also break heterolytically to produce high-valent metal species (Fe(IV), Co(IV)) through a two-electron transfer reaction [32]. To identify these ROS and evaluate their contribution to SMX degradation in the Co-Fe-Cube/PAA process, electron paramagnetic resonance (EPR) spectroscopy was used with 5,5-dimethyl-1-pyrrolineN-oxide (DMPO) and 2,2,6,6-tetramethyl-4-piperidinol (TEMP) as spin-trapping agents. Fig. 4a showed a legible DMPOX signal instead of DMPO-OH. The generation of DMPOX, an oxidized form of DMPO, could be ascribed to CH₃C(O)OO[•] with high redox potential, which was reported in previous Co-based PAA AOPs [37,38]. To further confirm the presence of RO[•], 2,2,6,6-tetramethyl-1-piperidinyloxy (TEMPO) was used as a radical trapping agent, and the signals of TEMPO-CH₃COO adduct (*m/z* 216.1594) were successfully detected in Fig. S13 [39]. Additionally, CH₃COO[•] could rapidly decompose to generate CH₃[•] via Eq. (8), and the TEMPO-CH₃ (*m/z* 172.1696) was also detected in Fig. S14 [21]. Hence, RO[•] are expected to play an important role in the Co-Fe-Cube/PAA process. PAA alone could generate ¹O₂ through the attack of central C atom by peroxy-group, which was confirmed by the TEMP-¹O₂ signal with a peak intensity ratio of 1:1:1 in Fig. 4b [40]. However, the signal intensity became weak after the addition of catalyst, demonstrating that the generation of ¹O₂ didn't get promoted in the PAA activation by Co-Fe-Cube.



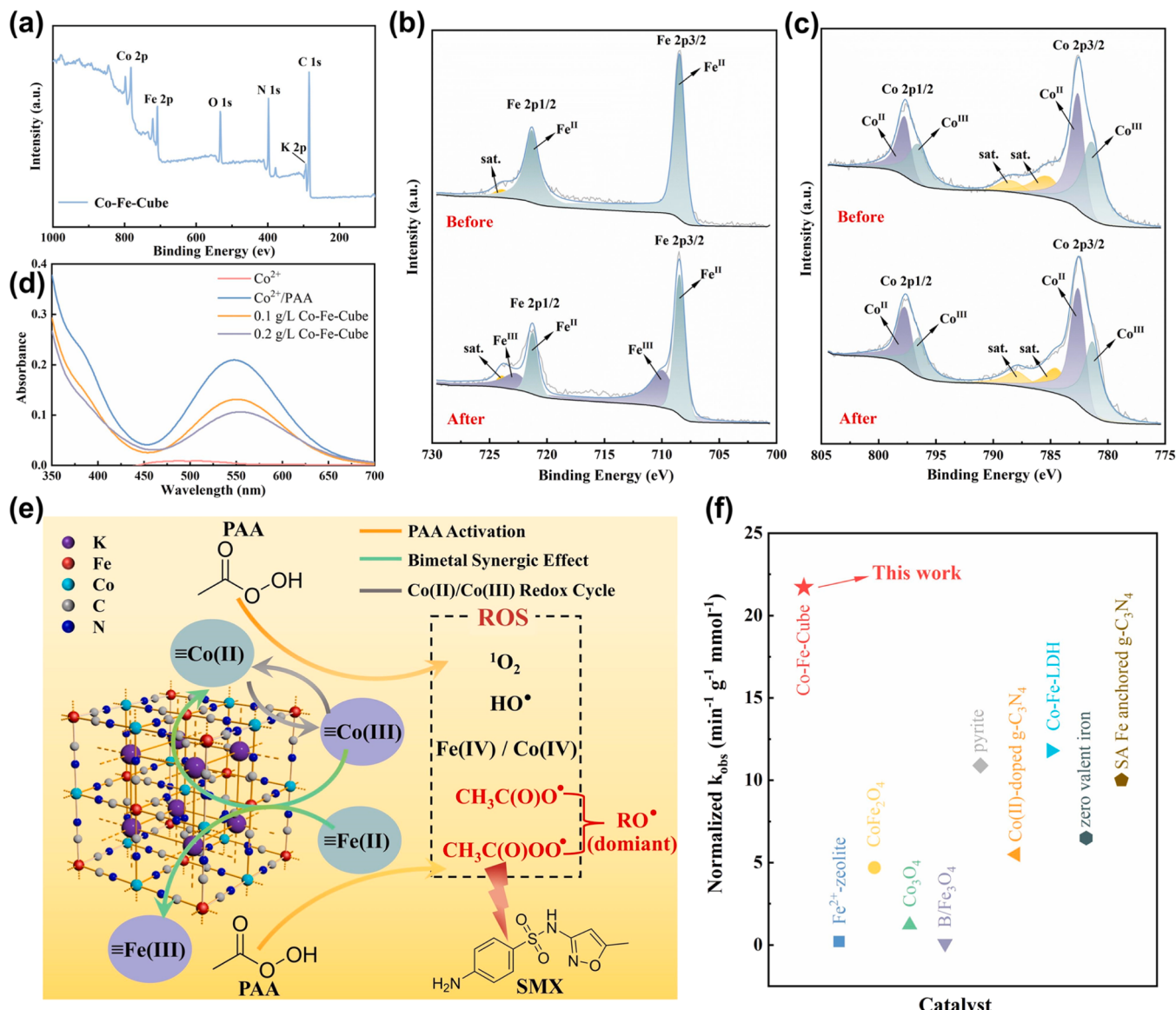
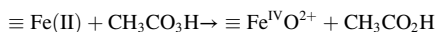
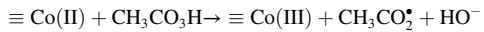


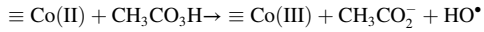
Fig. 5. (a) survey scan, (b) Fe 2p, and (c) Co 2p XPS spectra of Co-Fe-Cube before and after reaction. (d) UV-vis spectra of Co^{3+} -EDTA complex in Co^{2+} /PAA process with or without Co-Fe-Cube. (e) Proposed catalytic mechanism in the Co-Fe-Cube/PAA process. (f) Catalytic efficiency comparison of Co-Fe-Cube with previously reported catalysts in PAA activation (Table S4). Conditions: $[\text{Co}^{2+}] = 1 \text{ mM}$, $[\text{PAA}] = [\text{EDTA}] = 4 \text{ mM}$, temperature 25°C .



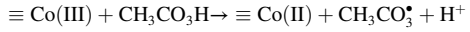
(3) $3.9 \mu\text{M}$ PMSO was degraded in 15 min when the initial concentration was $100 \mu\text{M}$, indicating that the steady concentration of Fe(IV) and Co(IV) in the Co-Fe-Cube/PAA process was quite low. Therefore, it seems that high valent metal species play a minor role in SMX removal. To determine the dominant ROS accounting for SMX removal in the Co-Fe-Cube/PAA process, quenching experiments were performed to figure out the specific contribution of multiple ROS. The commonly used *tert*-butyl alcohol (TBA) was selected to scavenge HO^{\bullet} ($k = 3.8\text{--}7.6 \times 10^8 \text{ M}^{-1} \text{ s}^{-1}$), and methanol (MeOH) was chosen to quench all ROS [43]. Additionally, PMSO could react with Fe(IV) or Co(IV) rapidly ($k = 10^5\text{--}10^6 \text{ M}^{-1} \text{ s}^{-1}$), which served as a quencher for high-valent metal species [42,44]. The results in Fig. 4d showed that 10 mM TBA only slightly affected the SMX degradation, suggesting the negligible contribution of HO^{\bullet} . The inhibiting effects caused by PMSO and MeOH were 19.3 % and 85.1 %, respectively, demonstrating that high-valent metal species play a minor role, while RO^{\bullet} is the dominant ROS contributing to SMX removal in the Co-Fe-Cube/PAA process.



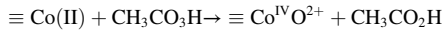
(4) The impact of common anions (HCO_3^2- , HPO_4^{2-} , Cl^-) and natural organic matters (represented as humic acid (HA)) was evaluated in



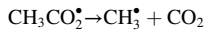
(5) Additionally, PMSO could react with Fe(IV) or Co(IV) rapidly ($k = 10^5\text{--}10^6 \text{ M}^{-1} \text{ s}^{-1}$), which served as a quencher for high-valent metal species [42,44]. The results in Fig. 4d showed that 10 mM TBA only slightly affected the SMX degradation, suggesting the negligible contribution of HO^{\bullet} . The inhibiting effects caused by PMSO and MeOH were 19.3 % and 85.1 %, respectively, demonstrating that high-valent metal species play a minor role, while RO^{\bullet} is the dominant ROS contributing to SMX removal in the Co-Fe-Cube/PAA process.



(6) The impact of common anions (HCO_3^2- , HPO_4^{2-} , Cl^-) and natural organic matters (represented as humic acid (HA)) was evaluated in



(7) The impact of common anions (HCO_3^2- , HPO_4^{2-} , Cl^-) and natural organic matters (represented as humic acid (HA)) was evaluated in



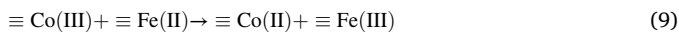
(8) The impact of common anions (HCO_3^2- , HPO_4^{2-} , Cl^-) and natural organic matters (represented as humic acid (HA)) was evaluated in

Methyl phenyl sulfoxide (PMSO) probe experiment was conducted in the Co-Fe-Cube/PAA process to identify the presence of high-valent metal species, which can undergo two-electron oxidation to generate methyl phenyl sulfone (PMSO₂) when it reacts with Fe(IV) or Co(IV) [41]. While hydroxylation products instead of PMSO₂ are produced by radicals (•OH , RO^{\bullet}) attack [42]. The generation of PMSO₂ was detected in Fig. 4c, and the yield rate ($\eta(\text{PMSO})$) was about 80 %, which demonstrated the presence of high valent metal species. However, only

Fig. S15. The addition of 1 mM Cl⁻ had insignificant effect on the SMX degradation, indicating a high tolerance of Cl⁻ in the Co-Fe-Cube/PAA process. The introduction of HCO₃⁻, HPO₄²⁻, and HA suppressed the SMX degradation to some extent, possibly due to their quenching effects on ROS [45,46]. Moreover, HCO₃⁻, HPO₄²⁻, and some carboxyl groups in HA might complex with \equiv Co and \equiv Fe to block the active sites, leading to the detrimental inhibition of PAA activation [37]. Increasing the PAA dosage was expected to take advantage of more catalytic sites and generate more RO[•]. By increasing the initial PAA concentration from 100 to 200 μ M in Fig. 4e and S16, the inhibition was alleviated, and more than 80 % SMX degradation was achieved. Moreover, the performance of Co-Fe-Cube/PAA process in actual water including tap water, secondary effluent and Yujia lake was investigated in Fig. 4 f. Co-Fe-Cube/PAA process could remove more than 70 % of SMX with PAA dosage of 200 μ M, manifesting the great applicability and excellent anti-interference of the Co-Fe-Cube/PAA process in practical application by choosing reasonable PAA and catalyst dosages.

3.5. Co-Fe bimetal synergic effect

\equiv Co and \equiv Fe bimetal both participate in the PAA activation as the catalytic sites, and they might exhibit a synergic effect to promote the catalytic performance [23,47,48]. As presented in Fig. S17, the Co-Co-PBA and Fe-Fe-PB with solid cubic feature were successfully prepared, and their catalytic performance was compared to Co-Fe-Cube in Fig. S18. The k_{obs} corresponding to Co-Fe-Cube was much higher than the sum of other two catalysts, demonstrating the bimetal synergic effect. The XPS spectra of fresh and used Co-Fe-Cube were used to further evaluate the interaction of bimetal active sites. Co, Fe, O, N, K, and C elements were present in Co-Fe-Cube, as observed in Fig. 5a, which was in agreement with the determined composition by EDS analysis (Fig. S5). The Fig. 5b exhibited the Fe 2p spectrum, and only the peaks representing \equiv Fe(II) existed at 708.4 and 721.3 eV, consistent with the PCET mechanism in Section 3.2. This indicated that all \equiv Fe(III) was reduced to \equiv Fe(II) via intramolecular electron transfer during the synthesis of Co-Fe-Cube. The new peaks that emerged after reaction at 710.0 and 722.8 eV were assigned to \equiv Fe(III), and 54.1 % of \equiv Fe(II) was oxidized to Fe(III), suggesting that Fe(II) participated in PAA activation. As indicated in Fig. 5c, the two peaks with binding energy at 781.3 and 796.5 eV represented Co(III), and the peaks at 782.6 and 797.7 eV were attributed to Co(II) in Co 2p3/2 and Co 2p1/2, respectively [49]. According to previous reports of Co-based materials in AOPs, the percentage of \equiv Co(II) is expected to decrease due to the faster reaction rate with PAA than \equiv Co(III) [21,23,37]. Surprisingly, an increase from 48.2 % to 55.3 % of \equiv Co(II) after the catalytic reaction was observed. To elucidate this phenomenon, the thermodynamically favorable reduction of \equiv Co(III) by \equiv Fe(II) via Eq. (9) was taken into consideration.



EDTA, a common complex agent, was used to evaluate the conversion of Co(III) to Co(II) in Fig. 5d and Text S9. The EDTA-Co(III) complex exhibits a typical absorption peak at 540 nm, which can be easily detected by UV-vis spectrophotometer [37]. No peak at 540 nm was observed in Co(II) alone, while the addition of PAA rapidly oxidized Co (II) to Co(III), and an apparent peak representing EDTA-Co(III) complex was clearly observed in Co(II)/PAA process. After adding 0.1 g L⁻¹ and 0.2 g L⁻¹ Co-Fe-Cube into the Co(II)/PAA process, the peak intensity decreased from 0.21 to 0.13 and 0.10, respectively, demonstrating the conversion of Co(III) to Co(II) by the \equiv Fe(II) sites on Co-Fe-Cube. Therefore, the \equiv Fe(II) active sites on the catalyst surface could not only activate PAA to generate ROS, but also induce the reduction of \equiv Co (III) to regenerate the highly active \equiv Co(II) sites toward PAA activation.

We summarized the catalytic mechanism of the Co-Fe-Cube/PAA process in Fig. 5e. The porous framework structure provides abundant active sites of \equiv Co(II), \equiv Co(III), and \equiv Fe(II), which efficiently activate

PAA to generate multiple ROS, including HO[•], high-valent metal species and RO[•]. Among these ROS, RO[•] is confirmed to play a dominant role. Both \equiv Co(II) and \equiv Co(III) rapidly react with PAA to form a Co(II)/Co (III) redox cycle. Furthermore, the Co-Fe bimetal synergic effect ensures the regeneration of highly active \equiv Co(II) sites, which greatly promotes the activation performance and the removal efficiency of SAs. To further substantiate the superiority of the state-of-the-art PBAs in heterogeneous catalysis, the Co-Fe-Cube/PAA process was compared with other PAA activation processes based on Co or Fe catalysts. A normalized k_{obs} is applied by dividing the k_{obs} with the PAA concentration and catalyst dosage, which reflects the ability and efficiency of catalysts to activate PAA and generate ROS [50]. As shown in Fig. 5 f, the Co-Fe-Cube/PAA process exhibited a much higher normalized k_{obs} (21.7 min⁻¹ g⁻¹ mmol⁻¹) than other processes (Table S4), demonstrating its remarkable catalytic activity.

3.6. Degradation pathway and biotoxicity evaluation

In order to assess the applicability of the Co-Fe-Cube/PAA process for practical water treatment, it's necessary to carefully investigate the degradation pathways and the biotoxicity of transformation products (TPs) [51]. LC-MS analysis identified eight TPs in the Co-Fe-Cube/PAA process, and their formulas, masses, and structures were listed in Table S5. Fig. 6a summarized the SMX degradation into three pathways. In pathway I, the electron-donating -NH₂ is vulnerable to electrophilic RO[•] and could be easily oxidized to the nitro byproducts (TP-270, TP-284) [23]. Additionally, N-centered radicals are proposed to generate via electron transfer, which further couple to form dimeric products (TP-503, TP-519, pathway II). The cleavage of the S-N bond of SMX also leads to the formation of TP-99 and TP-158, which can be further oxidized to TP-114 and TP-109, respectively (pathway III). All of these intermediates are expected to be transformed into small molecules, H₂O and CO₂ in the Co-Fe-Cube/PAA process.

The biotoxicity variation during SMX degradation is extremely important and should be evaluated carefully [52]. The Ecological Structure Activity Relationships (ECOSAR) program was applied to predict acute and chronic toxicity of SMX and eight TPs (Table S6). Fish, daphnid, mysid and green algae were chosen as the target organisms, and the logarithm of LC50, EC50, and Chv (Text S4) were presented in Fig. 6b. Most TPs show significantly lower biotoxicity than SMX, as evidenced by their higher logarithmic values with redder colors. Combing with the degradation pathways analyzed in Fig. 6a, biotoxicity is greatly attenuated in pathway I, while TP-503 and TP-519 in pathway II exhibit similar biotoxicity to SMX. Although TP-99 displays higher acute and chronic toxicity to daphnid and green algae in Fig. S20, its further degradation product and other TPs in pathway III exhibit much less harmful effects on the target organisms. It's worth noting that although the decreasing biotoxicity for most TPs was calculated, detecting all the TPs and measuring their actual concentrations during oxidation is quite difficult. In order to further test the overall variation of acute biotoxicity, *P. phosphoreum* T3 was selected, and its bioluminescence (L/L₀) was measured after exposure to the reaction solution for 15 min (details in Text S10) [38]. As presented in Fig. S21, the L/L₀ remained around 0.9, indicating that the biotoxicity variation of SMX and TPs during the entire reaction was not obvious, which confirmed the eco-friendly superiority of the Co-Fe-Cube/PAA process.

4. Conclusions

In this study, we employed a one-pot aqueous precipitation approach to construct Co-Fe-PBAs with diverse morphologies. As all the components of PBAs are non-toxic, low-cost, and earth abundant, their large-scale production for commercialization is feasible. The analyses based on structure-activity relationship demonstrated that the evolution of hollow interior leads to the partial destruction of the porous nanostructure as well as the catalytic activity, and Co-Fe-Cube exhibited the

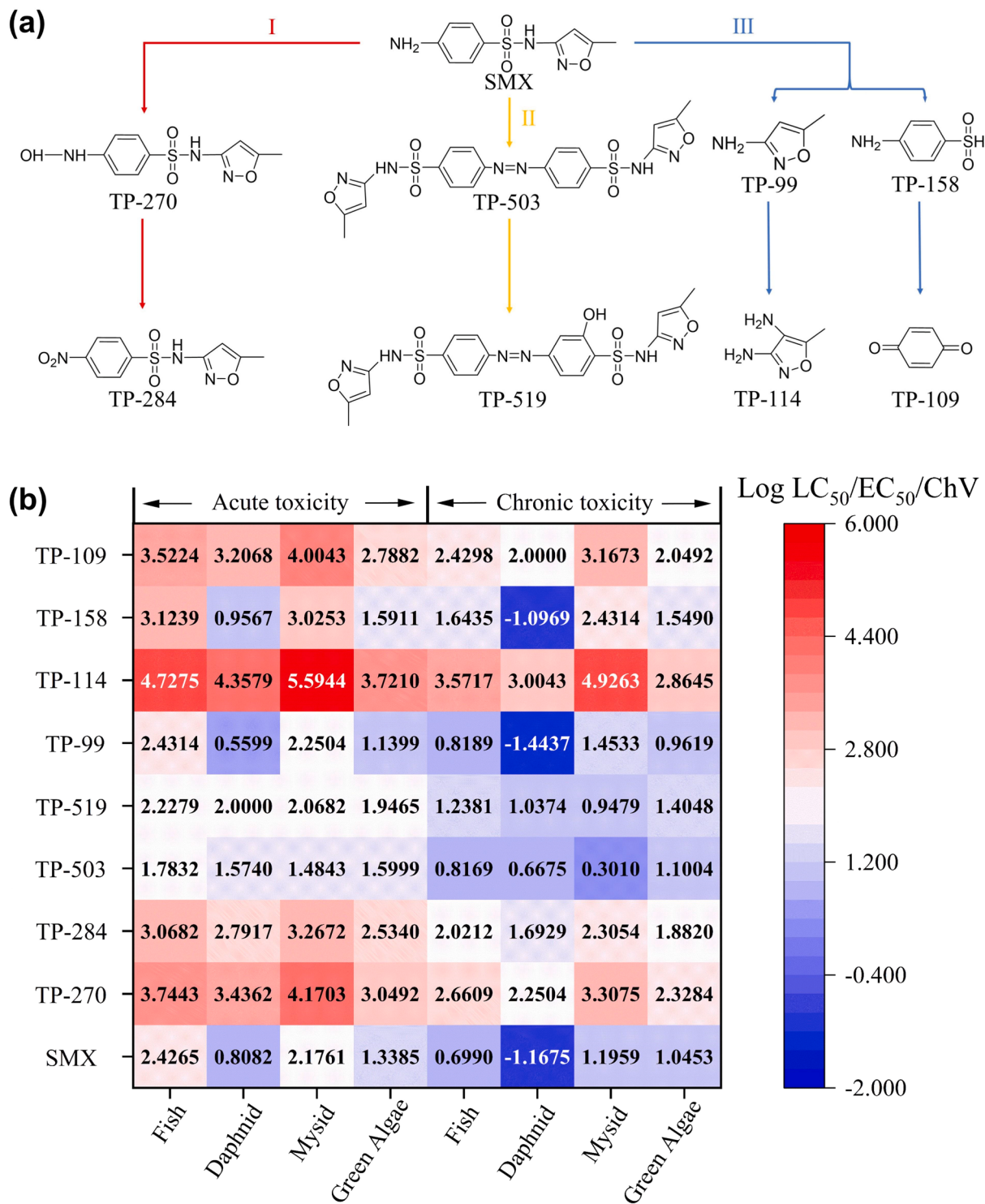


Fig. 6. (a) Proposed degradation pathways of SMX by PAA activation over Co-Fe-Cube. (b) Heat map of predicted toxicity of transformation products evaluated by ECOSAR program.

best performance in PAA activation, providing new insights into the intricate correlation between the material structure and the catalytic properties. The in-depth mechanism of the Co-Fe-Cube/PAA process was comprehensively studied by identifying the presence of multiple ROS, including HO[•], high-valent metal species, and RO[•], in which RO[•] is verified to be dominant. Co-Fe-Cube demonstrated excellent robustness and recyclability, as it retained its structural integrity and catalytic performance after four cycles. The Co-Fe-Cube owns several merits

including abundant active sites, anti-interference against water matrices, and Co-Fe bimetal synergic effect, thus ensuring the much higher catalytic efficiency toward PAA activation than previously reported Co or Fe-based materials. Additionally, transformation products of SMX were identified, and no increase in biotoxicity was observed, confirming the eco-friendly nature and bright prospects of the Co-Fe-Cube/PAA process. In practical water treatment, the recovery and reuse of Co-Fe-Cube can be achieved by its magnetic properties or

immobilization onto the substrates such as carbon material and membrane. Overall, the findings in our study highlights the importance of catalyst structure and morphology, thereby contributing to the progression of rational catalyst design in heterogeneous AOPs for water decontamination.

CRediT authorship contribution statement

Yujie Cheng: Conceptualization, Investigation, Data curation, Writing-Original draft, Formal analysis. **Zongping Wang:** Supervision, Methodology, Resources. **Lisan Cao:** Investigation, visualization. **Zhenbin Chen:** Data curation, Methodology. **Yiqun Chen:** Software, Methodology. **Zizheng Liu:** Software. **Jun Ma:** Resources. **Pengchao Xie:** Writing-review & editing, Project administration, Formal analysis, Funding acquisition, Resources.

Declaration of Competing Interest

The authors declare that they have no known competing financial interests or personal relationships that could have appeared to influence the work reported in this paper.

Data Availability

Data will be made available on request.

Acknowledgments

The supports by the National Natural Science Foundation of China (No. 5187308), the Young Top-notch Talent Cultivation Program of Hubei Province, and the Fundamental Research Funds for the Central Universities, HUST (grant 2022JYCXJJ029) are appreciated. We also thank the Analytical and Testing Center of Huazhong University of Science and Technology for related measurements.

Appendix A. Supporting information

Supplementary data associated with this article can be found in the online version at [doi:10.1016/j.apcatb.2023.123409](https://doi.org/10.1016/j.apcatb.2023.123409).

References

- [1] M. Qiao, G.G. Ying, A.C. Singer, Y.G. Zhu, Review of antibiotic resistance in China and its environment, *Environ. Int.* 110 (2018) 160–172, <https://doi.org/10.1016/j.envint.2017.10.016>.
- [2] J.M.A. Blair, M.A. Webber, A.J. Baylay, D.O. Ogbolu, L.J.V. Piddock, Molecular mechanisms of antibiotic resistance, *Nat. Rev. Microbiol.* 13 (2015) 42–51, <https://doi.org/10.1038/nrmicro3380>.
- [3] M. Patel, R. Kumar, K. Kishor, T. Mlsna, C.U. Pittman, D. Mohan, Pharmaceuticals of emerging concern in aquatic systems: chemistry, occurrence, effects, and removal methods, *Chem. Rev.* 119 (2019) 3510–3673, <https://doi.org/10.1021/acs.chemrev.8b00299>.
- [4] Y. Yang, Y.S. Ok, K.H. Kim, E.E. Kwon, Y.F. Tsang, Occurrences and removal of pharmaceuticals and personal care products (PPCPs) in drinking water and water/sewage treatment plants: a review, *Sci. Total Environ.* 596 (2017) 303–320, <https://doi.org/10.1016/j.scitotenv.2017.04.102>.
- [5] J. Lee, U. von Gunten, J.-H. Kim, Persulfate-based advanced oxidation: critical assessment of opportunities and roadblocks, *Environ. Sci. Technol.* 54 (2020) 3064–3081, <https://doi.org/10.1021/acs.est.9b07082>.
- [6] T. Zhang, T. Wang, B. Mejia-Tickner, J. Kissel, X. Xie, C.H. Huang, Inactivation of bacteria by peracetic acid combined with ultraviolet irradiation: mechanism and optimization, *Environ. Sci. Technol.* 54 (2020) 9652–9661, <https://doi.org/10.1021/acs.est.0c02424>.
- [7] T. Liu, S. Xiao, N. Li, J. Chen, X. Zhou, Y. Qian, C.H. Huang, Y. Zhang, Water decontamination via nonradical process by nanoconfined Fenton-like catalysts, *Nat. Commun.* 14 (2023), 2881, <https://doi.org/10.1038/s41467-023-38677-1>.
- [8] X.W. Ao, J. Eloranta, C.H. Huang, D. Santoro, W.J. Sun, Z.D. Lu, C. Li, Peracetic acid-based advanced oxidation processes for decontamination and disinfection of water: a review, *Water Res.* 188 (2021), 116479, <https://doi.org/10.1016/j.watres.2020.116479>.
- [9] Y.N. Shang, X. Xu, B.Y. Gao, S.B. Wang, X.G. Duan, Single-atom catalysis in advanced oxidation processes for environmental remediation, *Chem. Soc. Rev.* 50 (2021) 5281–5322, <https://doi.org/10.1039/d0cs01032d>.
- [10] L.M. Cao, D. Lu, D.C. Zhong, T.B. Lu, Prussian blue analogues and their derived nanomaterials for electrocatalytic water splitting, *Coord. Chem. Rev.* 407 (2020), 213156, <https://doi.org/10.1016/j.ccr.2019.213156>.
- [11] S.Z. Wang, C.M. McGuirk, A. d'Aquino, J.A. Mason, C.A. Mirkin, Metal-organic framework nanoparticles, *Adv. Mater.* 30 (2018), 1800202, <https://doi.org/10.1002/adma.201800202>.
- [12] M.B. Zakaria, T. Chikyow, Recent advances in Prussian blue and Prussian blue analogues: synthesis and thermal treatments, *Coord. Chem. Rev.* 352 (2017) 328–345, <https://doi.org/10.1016/j.ccr.2017.09.014>.
- [13] J.Y. Liu, X.N. Li, B. Liu, C.X. Zhao, Z.C. Kuang, R.S. Hu, B. Liu, Z.M. Ao, J.H. Wang, Shape-controlled synthesis of metal-organic frameworks with adjustable Fenton-like catalytic activity, *ACS Appl. Mater. Interfaces* 10 (2018) 38051–38056, <https://doi.org/10.1021/acsami.8b12686>.
- [14] N. Wang, W.J. Ma, Y.C. Du, Z.Q. Ren, B.H. Han, L.J. Zhang, B.J. Sun, P. Xu, X. J. Han, Prussian blue microcrystals with morphology evolution as a high-performance photo-Fenton catalyst for degradation of organic pollutants, *ACS Appl. Mater. Interfaces* 11 (2019) 1174–1184, <https://doi.org/10.1021/acsami.8b14987>.
- [15] J.W. Nai, X.W. Lou, Hollow structures based on Prussian blue and its analogs for electrochemical energy storage and conversion, *Adv. Mater.* 31 (2019), 1706825, <https://doi.org/10.1002/adma.201706825>.
- [16] X.N. Li, J.Y. Liu, A.I. Rykov, H.X. Han, C.Z. Jin, X. Liu, J.H. Wang, Excellent photo-Fenton catalysts of Fe-Co Prussian blue analogues and their reaction mechanism study, *Appl. Catal. B Environ.* 179 (2015) 196–205, <https://doi.org/10.1016/j.apcatb.2015.05.033>.
- [17] K.Y.A. Lin, H.K. Lai, S.P. Tong, One-step prepared cobalt-based nanosheet as an efficient heterogeneous catalyst for activating peroxyomonosulfate to degrade caffeine in water, *J. Colloid Interface Sci.* 514 (2018) 272–280, <https://doi.org/10.1016/j.jcis.2017.12.040>.
- [18] W.X. Zhang, H. Zhang, X. Yan, M. Zhang, R. Luo, J.W. Qi, X.Y. Sun, J.Y. Shen, W. Q. Han, L.J. Wang, J.S. Li, Controlled synthesis of bimetallic Prussian blue analogues to activate peroxyomonosulfate for efficient bisphenol A degradation, *J. Hazard. Mater.* 387 (2020), 121701, <https://doi.org/10.1016/j.jhazmat.2019.121701>.
- [19] N. Song, S.Y. Ren, Y. Zhang, C. Wang, X.F. Lu, Confinement of Prussian blue analogs boxes inside conducting polymer nanotubes enables significantly enhanced catalytic performance for water treatment, *Adv. Funct. Mater.* 32 (2022), 2204751, <https://doi.org/10.1002/adfm.202204751>.
- [20] J. Li, H. Yi, Y. Xiao, C. Liang, Y. Shen, Y. Li, Q. Fang, Freestanding catalytic membranes assembled from blade-shaped Prussian blue analog sheets for flow-through degradation of antibiotic pollutants, *Appl. Catal., B Environ.* 336 (2023), 122922, <https://doi.org/10.1016/j.apcatb.2023.122922>.
- [21] J.W. Wang, B. Xiong, L. Miao, S.L. Wang, P.C. Xie, Z.P. Wang, J. Ma, Applying a novel advanced oxidation process of activated peracetic acid by CoFe204 to efficiently degrade sulfamethoxazole, *Appl. Catal. B Environ.* 280 (2021), 119422, <https://doi.org/10.1016/j.apcatb.2020.119422>.
- [22] G. Zhou, Y. Fu, R. Zhou, L. Zhang, L. Zhang, J. Deng, Y. Liu, Efficient degradation of organic contaminants by magnetic cobalt ferrite combined with peracetic acid, *Process Saf. Environ. Prot.* 160 (2022) 376–384, <https://doi.org/10.1016/j.psep.2022.02.031>.
- [23] Z.H. Xie, C.S. He, Y.L. He, S.R. Yang, S.Y. Yu, Z.K. Xiong, Y. Du, Y. Liu, Z.C. Pan, G. Yao, B. Lai, Peracetic acid activation via the synergic effect of Co and Fe in CoFe-LDH for efficient degradation of pharmaceuticals in hospital wastewater, *Water Res.* 232 (2023), 119666, <https://doi.org/10.1016/j.watres.2023.119666>.
- [24] W. Zhang, H. Song, Y. Cheng, C. Liu, C. Wang, M.A.N. Khan, H. Zhang, J. Liu, C. Yu, L. Wang, J. Li, Core-shell prussian blue analogs with compositional heterogeneity and open cages for oxygen evolution reaction, *Adv. Sci.* 6 (2019), 1801901, <https://doi.org/10.1002/advs.201801901>.
- [25] J.W. Nai, J.T. Zhang, X.W. Lou, Construction of single-crystalline Prussian blue analog hollow nanostructures with tailorable topologies, *Chem* 4 (2018) 1967–1982, <https://doi.org/10.1016/j.chempr.2018.07.001>.
- [26] S. Cheng, C. Shen, H. Zheng, F. Liu, A. Li, OCNTs encapsulating Fe-Co PBA as efficient chainmail-like electrocatalyst for enhanced heterogeneous electro-Fenton reaction, *Appl. Catal. B Environ.* 269 (2020), 118785, <https://doi.org/10.1016/j.apcatb.2020.118785>.
- [27] J.W. Nai, B.Y. Guan, L. Yu, X.W. Lou, Oriented assembly of anisotropic nanoparticles into frame-like superstructures, *Sci. Adv.* 3 (2017), e1700732, <https://doi.org/10.1126/sciadv.1700732>.
- [28] S. Pintado, S. Goberna-Ferron, E.C. Escudero-Adan, J.R. Galan-Mascaros, Fast and persistent electrocatalytic water oxidation by Co-Fe Prussian blue coordination polymers, *J. Am. Chem. Soc.* 135 (2013) 13270–13273, <https://doi.org/10.1021/ja406242y>.
- [29] L. Ji, H.F. Zheng, Y.J. Wei, S.Q. Gong, T. Wang, S. Wang, Z.F. Chen, Temperature-controlled fabrication of Co-Fe-based nanoframes for efficient oxygen evolution, *Sci. China Mater.* 65 (2022) 431–441, <https://doi.org/10.1007/s40843-021-1743-7>.
- [30] D.R. Weinberg, C.J. Gagliardi, J.F. Hull, C.F. Murphy, C.A. Kent, B.C. Westlake, A. Paul, D.H. Ess, D.G. McCafferty, T.J. Meyer, Proton-coupled electron transfer, *Chem. Rev.* 112 (2012) 4016–4093, <https://doi.org/10.1021/cr200177j>.
- [31] P. Higel, F. Villain, M. Verdaguer, E. Riviere, A. Bleuzen, Solid-state magnetic switching triggered by proton-coupled electron-transfer assisted by long-distance proton-alkali cation transport, *J. Am. Chem. Soc.* 136 (2014) 6231–6234, <https://doi.org/10.1021/ja502294x>.
- [32] J. Kim, T.Q. Zhang, W. Liu, P.H. Du, J.T. Dobson, C.H. Huang, Advanced oxidation process with peracetic acid and Fe(II) for contaminant degradation, *Environ. Sci. Technol.* 53 (2019) 13312–13322, <https://doi.org/10.1021/acs.est.9b02991>.

[33] F. Chen, L.-L. Liu, J.-H. Wu, X.-H. Rui, J.-J. Chen, Y. Yu, Single-atom iron anchored tubular g-C₃N₄ catalysts for ultrafast Fenton-like reaction: Roles of high-valency iron-oxo species and organic radicals, *Adv. Mater.* 34 (2022), 2202891, <https://doi.org/10.1002/adma.202202891>.

[34] J.W. Wang, Z.P. Wang, Y.J. Cheng, L.S. Cao, F. Bai, S.Y. Yue, P.C. Xie, J. Ma, Molybdenum disulfide (MoS₂): a novel activator of peracetic acid for the degradation of sulfonamide antibiotics, *Water Res.* 201 (2021), 117291, <https://doi.org/10.1016/j.watres.2021.117291>.

[35] L.L. Zhang, J.B. Chen, Y.L. Zhang, Y. Xu, T.L. Zheng, X.F. Zhou, Highly efficient activation of peracetic acid by nano-CuO for carbamazepine degradation in wastewater: The significant role of H₂O₂ and evidence of acetylperoxy radical contribution, *Water Res.* 216 (2022), 118322, <https://doi.org/10.1016/j.watres.2022.118322>.

[36] Z.K. Xiong, Y.N. Jiang, Z.L. Wu, G. Yao, B. Lai, Synthesis strategies and emerging mechanisms of metal-organic frameworks for sulfate radical-based advanced oxidation process: a review, *Chem. Eng. J.* 421 (2021), 127863, <https://doi.org/10.1016/j.cej.2020.127863>.

[37] L.L. Zhang, J.B. Chen, Y.L. Zhang, Z.J. Yu, R.C. Ji, X.F. Zhou, Activation of peracetic acid with cobalt anchored on 2D sandwich-like MXenes (Co@MXenes) for organic contaminant degradation: high efficiency and contribution of acetylperoxy radicals, *Appl. Catal. B Environ.* 297 (2021), 120475, <https://doi.org/10.1016/j.apcatb.2021.120475>.

[38] Z.P. Wang, J.W. Wang, B. Xiong, F. Bai, S.L. Wang, Y. Wan, L. Zhang, P.C. Xie, M.R. Wiesner, Application of cobalt/peracetic acid to degrade sulfamethoxazole at neutral condition: efficiency and mechanisms, *Environ. Sci. Technol.* 54 (2020) 464–475, <https://doi.org/10.1021/acs.est.9b04528>.

[39] Y.J. Cheng, Z.P. Wang, J.W. Wang, L.S. Cao, Z.B. Chen, Y.Q. Chen, Z.Z. Liu, P.C. Xie, J. Ma, New insights into the degradation of micro-pollutants in the hydroxylamine enhanced Fe(II)/peracetic acid process: contribution of reactive species and effects of pH, *J. Hazard. Mater.* 441 (2023), 129885, <https://doi.org/10.1016/j.jhazmat.2022.129885>.

[40] Y. Gong, J. Shen, L. Shen, S. Zhao, Y. Wu, Y. Zhou, L. Cui, J. Kang, Z. Chen, Whose oxygen atom is transferred to the products? A case study of peracetic acid activation via complexed Mn(II) for organic contaminant degradation, *Environ. Sci. Technol.* 57 (2023) 6723–6732, <https://doi.org/10.1021/acs.est.2c09611>.

[41] Z. Wang, W. Qiu, S.-Y. Pang, Q. Guo, C. Guan, J. Jiang, Aqueous iron(IV)-oxo complex: an emerging powerful reactive oxidant formed by iron(II)-based advanced oxidation processes for oxidative water treatment, *Environ. Sci. Technol.* 56 (2022) 1492–1509, <https://doi.org/10.1021/acs.est.1c04530>.

[42] B.H. Liu, W.Q. Guo, W.R. Jia, H.Z. Wang, S.S. Zheng, Q.S. Si, Q. Zhao, H.C. Luo, J. Jiang, N.Q. Ren, Insights into the oxidation of organic contaminants by Co(II) activated peracetic acid: the overlooked role of high-valent cobalt-oxo species, *Water Res.* 201 (2021), 117313, <https://doi.org/10.1016/j.watres.2021.117313>.

[43] D. Kong, Y. Zhao, X. Fan, X. Wang, J. Li, X. Wang, J. Nan, J. Ma, Reduced graphene oxide triggers peracetic acid activation for robust removal of micropollutants: the role of electron transfer, *Environ. Sci. Technol.* 56 (2022) 11707–11717, <https://doi.org/10.1021/acs.est.2c02636>.

[44] Y. Bao, C. Lian, K. Huang, H.R. Yu, W.Y. Liu, J.L. Zhang, M.Y. Xing, Generating high-valent iron-oxo equivalent to Fe-IV=O complexes in neutral microenvironments through peroxyomonosulfate activation by Zn-Fe layered double hydroxides, *Angew. Chem. Int. Ed.* 61 (2022), e202209542, <https://doi.org/10.1002/anie.202209542>.

[45] L.S. Cao, J.W. Wang, Z.P. Wang, S.W. Yu, Y.J. Cheng, J. Ma, P.C. Xie, Inactivation of *Microcystis aeruginosa* by peracetic acid combined with ultraviolet: Performance and characteristics, *Water Res.* 208 (2022), 117847, <https://doi.org/10.1016/j.watres.2021.117847>.

[46] T. Luukkonen, U. von Gunten, Oxidation of organic micropollutant surrogate functional groups with peracetic acid activated by aqueous Co(II), Cu(II), or Ag(I) and geopolymer-supported Co(II), *Water Res.* 223 (2022), 118984, <https://doi.org/10.1016/j.watres.2022.118984>.

[47] F. Zhang, H.N. Yan, Y.F. Jin, L.F. Zhai, M. Sun, Co-Fe synergy in Co_xFe_{1-x}WO₄: the new type peroxyomonosulfate activator for sulfamethoxazole degradation, *Chem. Eng. J.* 461 (2023), 141989, <https://doi.org/10.1016/j.cej.2023.141989>.

[48] G.X. Huang, C.Y. Wang, C.W. Yang, P.C. Guo, H.Q. Yu, Degradation of bisphenol A by peroxyomonosulfate catalytically activated with Mn(1.8)Fe(1.2)O(4) nanospheres: synergism between Mn and Fe, *Environ. Sci. Technol.* 51 (2017) 12611–12618, <https://doi.org/10.1021/acs.est.7b03007>.

[49] R.O. Lezna, R. Romagnoli, N.R. de Tacconi, K. Rajeshwar, Cobalt hexacyanoferrate: compound stoichiometry, infrared spectroelectrochemistry, and photoinduced electron transfer, *J. Phys. Chem. B* 106 (2002) 3612–3621, <https://doi.org/10.1021/jp013991r>.

[50] Q.-Y. Wu, Z.-W. Yang, Z.-W. Wang, W.-L. Wang, Oxygen doping of cobalt-single-atom coordination enhances peroxyomonosulfate activation and high-valent cobalt-oxo species formation, *Proc. Natl. Acad. Sci. U. S. A.* 120 (2023), e2219923120, <https://doi.org/10.1073/pnas.2219923120>.

[51] J. Kuang, H. Guo, Q. Si, W. Guo, F. Ma, Nitrogen vacancies regulated the local electron density of iron sites in g-C₃N₄ to boost the generation of high-valent iron-oxo species in a peracetic acid-based Fenton-like process, *Appl. Catal. B Environ.* 337 (2023), 122990, <https://doi.org/10.1016/j.apcatb.2023.122990>.

[52] J.W. Wang, Y. Wan, J.Q. Ding, Z.P. Wang, J. Ma, P.C. Xie, M.R. Wiesner, Thermal activation of peracetic acid in aquatic solution: the mechanism and application to degrade sulfamethoxazole, *Environ. Sci. Technol.* 54 (2020) 14635–14645, <https://doi.org/10.1021/acs.est.0c02061>.